Published in final edited form as:
*Invest Ophthalmol Vis Sci*. 2003 September ; 44(9): 4061–4068. doi:10.1167/iovs.03-0124.

# Improved Contrast of Subretinal Structures using Polarization Analysis

**Stephen A. Burns**[1,2], **Ann E. Elsner**[1,2], **Mariane B. Mellem-Kairala**[1,2], and **Ruthanne B. Simmons**[2,3,4]

[1]The Schepens Eye Research Institute, Boston, Massachusetts

[2]Department of Ophthalmology, Harvard Medical School, Boston, Massachusetts

[3]Ophthalmic Consultants of Boston, Boston, Massachusetts

## Abstract

**PURPOSE—**To improve the ability to detect and quantify the early retinal changes associated with aging, age-related maculopathy, and age-related macular degeneration.

**METHODS—**A computational approach was implemented for analyzing images using a readily available polarimeter that is used for glaucoma diagnosis. This device, the GDx Nerve Fiber Analyzer (Laser Diagnostic Technologies, Inc., San Diego, CA), takes a series of images as a function of the polarization angle of the illuminating light. For each of 20 input polarizations, pairs of retinal images are digitized. One image is made of the light returning from the eye that is polarized parallel to the input light, and the other image is made of the light that is rotated by 90° from the input polarization. Using the raw data from these 40 images, and a simplified model of the polarization properties of the eye, we calculated the amount of light that returns in a parallel polarized state, and the amount of light that is depolarized by multiple scattering. Measurements were made in seven subjects with small drusen.

**RESULTS—**The depolarized light image produced a 3.4 times higher contrast of drusen and subretinal changes than the parallel polarized light images.

**CONCLUSIONS—**Polarization-sensitive imaging combined with a simple computational approach allows the measurement of the retinal distribution of multiply scattered light. With this technique, retinal imaging of age-related changes in retinal and subretinal tissue can be improved.

Age-related macular degeneration (AMD) is the leading cause of blindness in the adult population of the United States.[1] In AMD, the diseased tissues lie beneath the highly reflective vitreoretinal interface, plus many layers of other retinal cells, making it difficult to visualize the early changes in this disease. As a result, the reported incidence of subretinal changes both in patients with AMD and in aged normal subjects is much higher in histologic studies than in clinical and epidemiologic studies. Histology has been used to show that the early stages of AMD are marked by thickening of Bruch's membrane, the development of basal linear deposits,[2–5] and the development of drusen too small to be detected clinically. [6–10] Widespread or diffuse subretinal changes have been conclusively shown to occur long before donors have reached the age associated with clinical disease.[6,9] These findings, together with the extremely

[4]Deceased.



Corresponding author: Stephen A. Burns, The Schepens Eye Research Institute, 20 Staniford Street, Boston, MA 02114; sburns@vision.eri.harvard.edu.

Disclosure: **S.A. Burns**, (P); **A.E. Elsner**, (P); **M.B. Mellem-Kairala**, None; **R.B. Simmons**, None

gradual progression of early stages, suggest that age-related maculopathy (ARM) and AMD may begin during middle age, if not sooner. Accurate assessment and improved quantification of early stages of the disease is of growing importance for studies of affected family members and evaluating the effectiveness of proposed earlier treatments, such as vitamin supplementation.[11]

In ARM, direct measurement of these early changes to the RPE and Bruch's membrane is difficult because of the relatively low contrast of small drusen and other subretinal deposits, especially in the presence of age-related decreases in lens transparency and pupil size. In recent years, infrared imaging has been used to improve the visibility of subretinal changes such as drusen and hyperpigmentation in both middle-aged and elderly subjects without clinical signs of disease.[12,13] There is excellent spatial correspondence of drusen appearing on infrared images with the drusen that appeared in images produced by other methods.[14] These advanced digital imaging techniques have been used successfully, with large numbers of patients in a clinical setting.[15,16] Thus, although infrared confocal imaging has been shown to be superior to color fundus imaging (Miura M, et al. *IOVS* 2001;42:ARVO Abstract 3800),[17] the standard method for most clinical studies remains color fundus photography because of the lack of reliable commercial instrumentation.

Detection of disease by imaging is a problem of determining the most relevant properties of the tissue of interest and then optimizing the technique. A simple model of the optical properties of the healthy human retina and RPE consists of a stack of layers containing well-ordered and contiguous cells and their processes,[18] but this model fails to describe a retina with ARM or AMD. As the disease progresses, Bruch's membrane thickens.[4,7,17–21] It becomes less ordered, and as a result there is an overall increase in light scattering from this layer.[12] On a finer scale there are features such as drusen, hyperpigmentation, pigment clumping, and eventually atrophy or exudation. These changes occur beneath the brighter neural layers of the retina, which return a high proportion of light, which has been either specularly reflected or singly scattered. Thus, in the early stages of the disease, the total amount of scattered light returned to the detector is relatively low, and standard imaging modalities do not provide a high-contrast image of early changes, even with near infrared light and confocal imaging. Sampling multiply scattered light and eliminating the directly backscattered light causes the deeper layers and pathologic tissues to be viewed in increased contrast.[12–14,16,22–23]

To form an image using multiply scattered light, the primary method has been to minimize the directly backscattered light in a confocal scanning laser ophthalmoscope (SLO)[25] by the use of an annular aperture and infrared illumination.[12,26] Other techniques have also been developed to form an image from multiply scattered light—for instance, by displacing the light source out of alignment with the confocal aperture, as in multiply scattered light tomography.[16] The current work tests the use of polarimetry for forming a retinal image from predominantly multiply scattered light and compares the resultant contrast to images formed from directly backscattered light. Light that is singly scattered off superficial layers retains polarization, whereas light that has been scattered multiple times becomes depolarized.[27,28] By removing the polarization-preserving component of the light returning from the ocular fundus, regardless of the source, it is possible to calculate the spatial distribution of the multiply scattered (i.e., depolarized) light on a pixel-by-pixel basis[29–33] (Burns, et al. *IOVS* 2001;42: ARVO Abstract 3808; Mellem-Kairala M, et al., *IOVS* 2002;43: ARVO E-Abstract 245), to test the hypothesis that contrast of subretinal features is increased for depolarized light imaging.

# METHODS

## Subjects

We selected 7 patients who had subretinal features of interest, 5 women and 2 men, aged 46 to 61 years (Table 1), from 13 patients who were undergoing polarimetry testing for peripapillary changes. Patients had glaucoma or suspected glaucoma, with IOP less than 25 mm Hg controlled by topical medicines. Visual acuity was 20/60 or better, with ametropia less than 6 D. We excluded patients with previous eye trauma or surgery in one or both eyes, except for cataract extraction and other eye diseases such as diabetic retinopathy or AMD. We chose to sample subjects with primary open-angle glaucoma because they had been thoroughly screened and were age appropriate for development of small drusen and other signs of the small, early changes preceding AMD.

All patients underwent a complete ophthalmic examination by two glaucoma specialists, including visual acuity, slit lamp biomicroscopy, and indirect ophthalmoscopy. The intraocular pressure was measured in all patients in a standardized manner by trained technicians using a slit lamp–mounted applanation tonometer. Automated perimetry and 30° color fundus photography were performed as indicated clinically. After a detailed oral explanation of the study procedure, informed consent was obtained from all participants in a protocol approved by the Institutional Review Board of the Schepens Eye Research Institute. The research conformed to the tenets of the Declaration of Helsinki.

## Equipment

We used data from a commercially available ellipsometer, a type of polarimeter, the GDx Nerve Fiber Analyzer (Laser Diagnostic Technologies, Inc., San Diego, CA), which was originally developed for measuring the thickness of the nerve fiber layer.[35,36] This instrument is a confocal SLO that also analyzes the effect of the traversal of light through the eye on the polarization state of the light. Linearly polarized laser light at 780 nm scans the retina in a raster pattern covering 15° visual angle. The angle of polarization is controlled by a rotating half-wave plate. Light returning from the eye is then used to form two sets of images: one from a detector that collects light of the same polarization as the illumination light (the parallel polarized light) and one from a detector that collects the linearly polarized light at 90° to the illumination light (the perpendicularly polarized light). In each image series, 20 pairs of images are generated in less than 1 second, where image pairs differ in the angle of the illumination polarization. Each image in the series is saved as 256 × 256 pixels with 8 bits of gray scale, using a linear detection system.

The instrument also includes a corneal compensator placed between the eye and the half-wave plate. The corneal compensator is a birefringent element, designed to counter the average birefringence of the cornea.[36–40] Our analysis technique differs from existing approaches. We use the polarization information to obtain a map of the multiply scattered light returning from the retina to enhance detection of pathologic features, rather than performing measurements to determine nerve fiber layer thickness using the retardance at a given fundus location.[41,42] The display of the latter renders nearly invisible the fundus features from the deeper layers.

## Procedures

Infrared scanning laser polarimetry was performed without pupil dilation at the Ophthalmic Consultants of Boston. Six image series were acquired from each eye: three using a standard gain setting for the instrument and three with varying gain (one lower gain and two higher gains than the standard). The raw data, which are not typically available, were saved to hard disc and then transferred to a laboratory computer at the Schepens Eye Research Institute for further analysis.

## Polarization Computations

We processed the raw data from the GDx image series to generate images representing the principle optical properties of the returning light[29,33] (Burns SA, et al. *IOVS* 2001;42:ARVO Abstract 3808; Mellem-Kairala M, et al. *IOVS* 2002;43:ARVO E-Abstract 245). We developed a set of routines in commercial software (MatLab; The Mathworks, Natick, MA) to use with the 20 pairs of raw images (Burns SA, et al. *IOVS* 2001;42:ARVO Abstract 3808).[29] For simplicity the analysis assumes that the major factor altering polarization properties in the retina is the linear birefringence of the nerve fiber layer. As the cornea of the eye is also birefringent, we used the average corneal compensation provided by the commercially available GDx, although future work could benefit from the individual compensation recently developed[40,43] (see the Discussion section). The other major factor altering the polarization properties of light in the retina is then assumed to be multiple scattering, which depolarizes light.[27,28] Thus, light returning through the pupil from the retina can be classified along a continuum that depends on how polarized the sampled light is. This can be quantified by separating the light into two components. One component is light that has been specularly reflected, or at most scattered only a few times, and thus retains its polarization. The second component is light that has been multiply scattered and thus has lost its polarization.

Because the retina is birefringent,[34,44,45] separating these components requires the application of polarimetric analysis (Dreher AW, et al. *IOVS* 1992;33:ARVO Abstract 968).[30,32,37,38,46–48] Although a full description of the polarization properties requires the measurement of sufficient independent conditions to specify all possible parameters of polarization, detailed analyses of partial polarimetry in the eye, such as that performed by the GDx, have been described that allow comparison to the full model.[31,38]

Figure 1 shows the difference across images obtained for each of the two detectors of the GDx, for 4 of the 20 input polarization angles. On the left of Figure 2 is shown one image pair, with a region of interest indicated on the images. On the right, the average grayscale value within this 3 × 3-pixel region of interest is plotted as a function of input polarization. As expected[30,31] the intensity of the pixel varied approximately sinusoidally as the input angle of polarization was rotated. The angle of the retinal birefringence is represented by the phase of this curve. This phase varied with retinal position, because the nerve fiber layer varies in orientation across the retina. The minimum in the crossed detector intensity function represents the angle for which the incoming light is aligned with either the fast or slow axis of the retinal birefringence. At this location the only light that gets to the crossed detector is light that has undergone an alteration of the polarization properties, such as having been depolarized by multiple scattering or otherwise changed in its polarization state. To determine the retinal distribution of the multiple retinal scattering in a system that contains chiefly linear birefringent elements, it is therefore necessary only to find the minimum intensity for each pixel.

The grayscale value of each image in the image series was corrected by using the spatially resolved offset and gain calibrations provided with each instrument. Next, all images were aligned to correct for eye movements. We then calculated image types representing a particular aspect of the reflectance of the retina.

First, we computed the distribution of depolarized light (the depolarized light image), which is the minimum value of light detected for the crossed detector and all input polarization angles.

$$I_{\mathrm{DP}} = \min[\mathrm{F}(\alpha)] \tag{1}$$

where $I_{\mathrm{DP}}$ is the depolarized light intensity at that pixel, F is the intensity function of the crossed detector for all images in a set, α is the angle of input polarization, and min is the minimum of

the function. Note that this value represents the estimate of half the amount of depolarized light returning from the retina at a given location.

Second, we computed the parallel polarized light image as the average intensity for the parallel polarized light minus the depolarized light contribution at each pixel ($I_{DP}$).

$$I_{PP}=(\Sigma(PPD_i))/20 - I_{DP} \quad (2)$$

where $I_{PP}$ is the parallel polarized light intensity at that pixel, PPD (i = 1,20) is the total intensity for the parallel polarized detector and $I_{DP}$ is as just described. This value represents the average amount of light that retains its original polarization, independent of input polarization.

Third, we calculated the grand mean of the light returning to both detectors for all input polarization states.

$$I_{M}=(\Sigma(PPD_i+DPD_i))/40 \quad (3)$$

where $I_M$ is the light intensity at each pixel averaged across images, PPD is the light intensity for the parallel polarized detector, and DPD the intensity distribution for the perpendicularly polarized detector (i = 1,20). This value represents the average relative reflectance of the retina, or conversely the relative reflectance that would be measured with a polarization insensitive detection channel and a randomly polarized light source. This image is what is obtained with a typical confocal SLO.

Finally, for comparison to the GDx output, we calculated the polarization modulation amplitude image, or $I_{PMA}$, which represents input polarization dependent change in intensity, as

$$I_{PMA}=\max[F(\alpha)] - \min[F(\alpha)] . \quad (4)$$

This image represents, as high-intensity, regions of the retina where the polarization of the returning light is most dependent on the polarization of the illumination light.

For these images, although the intensities vary markedly, with $I_{DP}$ typically being the smallest, the expected proportion of multiply scattered light from most to least is $I_{DP} > I_M > I_{PP}$. All the images to be shown are scaled for visibility of small features in a print format. Thus, the actual intensities, although used in all computations, are not shown in the figures, because $I_{DP}$ is small in comparison to $I_{PP}$ in relatively normal eyes.

## Calculation of Contrast

Features consistent with subretinal changes[12] were identified by one of the investigators (SAB) in the depolarized, average, and parallel polarized images. To qualify as a feature of interest, the subretinal feature had to appear in at least one type of computed image and all three standard image sets and not be spatially contiguous with other features that could be confounded, such as blood vessels, hyperpigmentation, atrophy, or the optic nerve head. This selection was also compared to the color fundus photographs for the same criteria. The average intensity of a 3 × 3-pixel region of the retina for each selected feature was calculated, and the average intensity of the same size region adjacent to the feature was also calculated. These values were calculated from the same locations of all images. From these intensities the Michelson contrast, a metric used to quantify contrast for specific features that minimizes unrelated grayscale changes, was calculated as

$$\text{Contrast}=(I_{\text{feature}} - I_{\text{adjacent}})/(I_{\text{feature}}+I_{\text{adjacent}}) \quad (5)$$

where $I_{\text{feature}}$ was the average grayscale value on the feature and $I_{\text{adjacent}}$ was the average grayscale value next to the feature, but avoided obvious features such as blood vessels. Because the number of features varied markedly from eye to eye, we chose to score only three locations per eye, allowing parametric statistics with a balanced design.

To control for possible artifacts of image processing that could cause systematic changes in contrast for each image type we also computed contrasts for arbitrarily chosen regions in the image. First, a region without major retinal features was selected by the operator on the retinal image. Next, a computer processing routine (MatLab; The MathWorks) picked a series of adjacent pairs of regions (without further user interaction). The number of regions was dependent on the size of the region chosen, which was primarily dependent on the ability to find a region without retinal vessels or other readily visible features. The brighter region of each pair was designated as a “feature,” and the adjacent darker region as the “background.” Contrast for each image type was then automatically calculated as described earlier.

## RESULTS

The computed images are distinctly different from one another and appeared to represent accurately the expected difference in image qualities. Figure 3 compares computed images to the standard image computations from the GDx and to the color fundus photograph for an eye from our sample. Although a large druse (the yellowish spot indicated by the arrow) was visible in the color fundus photograph (Fig. 3A), it was more visible in all the infrared images (Figs. 3B, 3D, 3E) except the GDx birefringence image (Fig. 3C) and the polarization modulation image (Fig. 3F). The contrast of this spot was highest in the depolarized light image. This was true for all drusen that were identifiable in the corresponding color images. Figure 4 and Figure 5 compare the three main calculated image types for two additional eyes. The polarization modulation images emphasize only regions of polarization preserving light return and birefringence, and are therefore not shown further.

The depolarized light image $I_{\text{DP}}$ (Fig. 4A, Fig 5A) differed greatly in appearance from any of the raw images from which each was derived. There were striking grayscale changes across the retina, corresponding to relatively more and less preservation of polarized light. The portions of the image that appeared brighter indicate that more depolarized light is returned at this retinal location compared with other locations. Conversely, darker portions of the image indicate regions for which less depolarized light is returned, compared with the adjacent fundus. Some of the darkest structures were the retinal blood vessels, which appeared fairly wide and darkest in their central portions. The choroidal rim of the optic nerve head was also revealed.

In contrast, the parallel polarized light images shows features consistent with specularly reflected light (Fig. 4B, Fig 5B). Blood vessels show the characteristic brighter central stripes due to specular reflection from the curved surface of the vessel and the surface features of the retina, such as nerve fiber bundles are more visible, than in the depolarized light images.

The average relative reflectance images (Fig. 4C, Fig 5C) were, as expected, intermediate between the parallel polarized and depolarized light images. The blood vessels were striped, with brighter centers and darker edges, as is typical of confocal images. This is indicative of some portion of the light returning in a specular manner, but these images represent a mixture of the depolarized and polarization preserving information.

### Contrast of Subretinal Features

Because the relative proportion of multiply scattered light is expected to vary across images, our initial hypothesis was that the depolarized light images would have the highest contrast, the average images next, and the parallel polarized light images the least contrast. The average contrast of the features were 0.142 (depolarized light), 0.051 (average relative reflectance), and 0.031 (parallel polarized light). The control regions did not show this significant change in contrast. The average contrast of the control regions was 0.019 (depolarized light), 0.004 (average relative reflectance), and −0.015 (parallel polarized light). The difference between the depolarized light contrast and the other two conditions was significant ($P < 0.0033$, ANOVA), but differences for control conditions were not significant ($P > 0.05$).

Figure 6 shows the contrast of subretinal features in the images. Figure 6A compares the measured Michelson contrast of subretinal features for depolarized light and the average relative reflectance images for each eye in the study. Increased contrast for the depolarized light image is represented by points lying above the diagonal line; all points lie well above the line. Figure 6B shows the average contrast in each of the three selected features in all three calculated images, summarizing the data for all patients, with each patient having equal weight whether one or two eyes were tested. Again, the increased contrast for the depolarized light images is readily apparent.

## DISCUSSION

The identification and quantification of early changes in ARM and AMD is difficult, and limits clinical trials and research studies. Although there are a number of both functional (Klein R, et al. *IOVS* 1997;38:ARVO Abstract 2186).[49–55] and imaging modalities[12,56–59] that can show reliable early changes in ARM, they have been limited by either long testing times or lack of availability. The technique we presented uses a standard clinical instrument and produces marked increases in the detect-ability of small subretinal changes in eyes without AMD, providing a potential methodology that is more widely available for larger patient sets.

Polarization has been used to improve contrast in biological imaging, and crossed polarizers have been used widely to increase contrast in the presence of scattering.[28,60–62] The scanning laser polarimeter was designed to extract more information than a fixed set of polarization generation and analysis components, because the nerve fiber bundles are well known to exhibit different thicknesses and orientations across the macula.[35,41,46,63,64] Although in principle the GDx, because it does not measure the complete Müller matrix, can produce erroneous results, the major sources of error for our application would probably be corneal birefringence (see below) or diattenuation. Diattenuation is not considered a major problem, because there is little diattenuation in the retina in the near infrared.[34] Recently, polarimetry using the full Müller matrix model to characterize all parameters has also been used to optimize retinal contrast.[32] This approach has the advantage over the GDx of obtaining the complete Müller matrix of the retina. However, the optimization technique finds the polarization vector that produces the highest retinal contrast, typically the reflective retinal features, instead of the lower contrast subretinal features of the current work.

The current analysis provides images based primarily on the distribution of multiply scattered light in the retinal image, by using the depolarized light to compute a new image. We have shown that both indirect imaging with the confocal SLO[12,14] and multiply scattered light tomography[22,23] also provide this type of information, although these retinal imaging modalities are not as widely available as the GDx. However, these studies have also shown that scattered light imaging is an excellent technique for looking at other pathologic changes in the retina, including neovascularization,[12,14,65,66] macular cysts,[67] pigment epithelial

detachments,[21] and retinal edema.[68,69] Thus, the applicability of the proposed technique may extend beyond imaging of early AMD.

One potential problem with the simple calculations we have presented is that the cornea of the human eye is also birefringent.[36,39,44,62,70–73] It has recently been shown that marked improvements in the reliability of nerve fiber layer thickness estimates across a population are obtained by using individualized compensation of corneal birefringence. [40,43,40,74] The present study did not individually compensate the corneal polarization. Because the GDx is an incomplete polarimeter, it can overestimate the distribution of depolarized light.[31] The potential improvement of using individualized compensation remains to be investigated, but we expect it to be relatively small. In addition to improved control of the polarization of the system, other technical improvements could be made to further increase the accuracy of the measurements. The dynamic range of the instrument must accommodate a large range of intensities returning from the retina. Because the amount of depolarized light in healthy eyes is relatively low, it is important to obtain images that are bright, without saturating the detectors. For this reason, it may be desirable to digitize the retinal images with a wider dynamic range.

In conclusion, we have shown that using a widely available clinical imaging device the GDx Nerve Fiber Analyzer and relatively simple software, it is possible to improve markedly the imaging of subretinal changes. The use of this technique holds promise for improved quantification of the early changes in aging, ARM, and AMD.

## Acknowledgment

The authors thank the Ophthalmic Consultants of Boston for the use of their instrument and assistance with patient coordination.

Supported by Grants EY07624 and EY04395 from the National Eye Institute and the Saltonstall Foundation (AEE).

## References

1. Leibowitz HM, Krueger DE, Maunder LR, et al. The Framingham Eye Study monograph: an ophthalmological and epidemiological study of cataract, glaucoma, diabetic retinopathy, macular degeneration, and visual acuity in a general population of 2631 adults, 1973–1975. Surv Ophthalmol 1980;24:335–610. [PubMed: 7444756]
2. Feeney-Burns L, Ellersieck MR. Age-related changes in the ultra-structure of Bruch's membrane. Am J Ophthalmol 1985;100:686–697. [PubMed: 4061550]
3. Ramrattan RS, van der Schaft TL, Mooy CM, de Bruijn WC, Mulder PG, de Jong PT. Morphometric analysis of Bruch's membrane, the choriocapillaris, and the choroid in aging. Invest Ophthalmol Vis Sci 1994;35:2857–2864. [PubMed: 8188481]
4. Spraul CW, Lang GE, Grossniklaus HE. Morphometric analysis of the choroid, Bruch's membrane, and retinal pigment epithelium in eyes with age-related macular degeneration. Invest Ophthalmol Vis Sci 1996;37:2724–2735. [PubMed: 8977488]
5. Starita C, Hussain AA, Patmore A, Marshall J. Localization of the site of major resistance to fluid transport in Bruch's membrane. Invest Ophthalmol Vis Sci 1997;38:762–767. [PubMed: 9071230]
6. Lewis H, Straatsma BR, Foos RY. The prevalence of macular drusen in postmortem eyes. Am J Ophthalmol 1986;102:801–803. [PubMed: 3789064]
7. Green WR, McDonnell PJ, Yeo JH. Pathologic features of senile macular degeneration. Ophthalmology 1985;92:615–627. [PubMed: 2409504]
8. Sarks JP, Sarks SH, Killingsworth MC. Evolution of geographic atrophy of the retinal pigment epithelium. Eye 1988;2:552–577. [PubMed: 2476333]
9. Green WR, Enger C. Age-related macular degeneration histopathologic studies. The 1992 Lorenz E. Zimmerman Lecture. Ophthalmology 1993;100:1519–1535. [PubMed: 7692366]

10. Sarks SH, Arnold JJ, Killingsworth MC, Sarks JP. Early drusen formation in the normal and aging eye and their relation to age related maculopathy: a clinicopathological study. Br J Ophthalmol 1999;83:358–368. [PubMed: 10365048]
11. Kassoff A, Kassoff J, Buehler J, et al. A randomized, placebo-controlled, clinical trial of high-dose supplementation with vitamins C and E, beta carotene, and zinc for age-related macular degeneration and vision loss: AREDS Report No. 8. Arch Ophthalmol 2001;119:1417–1436. [PubMed: 11594942]
12. Elsner AE, Burns SA, Weiter JJ, Delori FC. Infrared imaging of sub-retinal structures in the human ocular fundus. Vision Res 1996;36:191–205. [PubMed: 8746253]
13. Elsner AE, Burns SA, Beausencourt E, Weiter JJ. Foveal cone photopigment distribution: small alterations associated with macular pigment distribution. Invest Ophthalmol Vis Sci 1998;39:2394–2404. [PubMed: 9804148]
14. Hartnett ME, Elsner AE. Characteristics of exudative age-related macular degeneration determined in vivo with confocal and indirect infrared imaging. Ophthalmology 1996;103:58–71. [PubMed: 8628562]
15. Kelley LM, Walker JP, Wing GL, Raskauskas PA, Elsner AE. Scanning laser ophthalmoscope imaging of age related macular degeneration and neoplasms. J Ophthalmic Photogr 1997;3:89–94.
16. Elsner AE, Miura M, Burns SA, et al. Multiply scattered light tomography and confocal imaging: detecting neovascularization in age-related macular degeneration. Optics Express 2000;7:95–106. [PubMed: 19404374]
17. Ishiko S, Akiba J, Horikawa Y, Yoshida A. Detection of drusen in the fellow eye of Japanese patients with age-related macular degeneration using scanning laser ophthalmoscopy. Ophthalmology 2002;109:2165–2169. [PubMed: 12414434]
18. Delori FC, Pflibsen KP. Spectral reflectance of the human ocular fundus. App Opt 1989;28:1061–1077.
19. Curcio CA, Millican CL, Bailey T, Kruth HS. Accumulation of cholesterol with age in human Bruch's membrane. Invest Ophthalmol Vis Sci 2001;42:265–274. [PubMed: 11133878]
20. Hageman GS, Luthert PJ, Victor Chong NH, Johnson LV, Anderson DH, Mullins RF. An integrated hypothesis that considers drusen as biomarkers of immune-mediated processes at the RPE-Bruch's membrane interface in aging and age-related macular degeneration. Prog Retinal Eye Res 2001;20:705–732.
21. Spraul CW, Grossniklaus HE. Characteristics of drusen and Bruch's membrane in postmortem eyes with age-related macular degeneration. Arch Ophthalmol 1997;115:267–273. [PubMed: 9046265]
22. Elsner AE, Dreher A, Beausencourt E, Burns S, Zhou Q, Webb RH. Multiply scattered light tomography: vertical cavity surface emitting laser array used for imaging subretinal structures. Lasers Light Ophthalmol 1998;8:193–202.
23. Kunze C, Elsner AE, Beausencourt E, Moraes L, Hartnett ME, Trempe CL. Spatial extent of pigment epithelial detachments in age-related macular degeneration. Ophthalmology 1999;106:1830–1840. [PubMed: 10485559]
24. Elsner AE, Zhou Q, Beck F, et al. Detecting AMD with multiply scattered light tomography. Int Ophthalmol 2001;23:245–250. [PubMed: 11944848]
25. Webb RH, Hughes GW, Delori FC. Confocal scanning laser ophthalmoscope. Appl Opt 1987;26:1492–1499.
26. Elsner AE, Burns SA, Webb RH, Hughes GW. Reflectometry with a scanning laser ophthalmoscope. Appl Opt 1992;31:3697–3710.
27. Jarry G, Steimer E, Damaschini V, Epifanie M, Jurczak M, Kaiser R. Coherence and polarization of light propagating through scattering media and biological tissues. Appl Opt 1998;37:7357–7367. [PubMed: 18301570]
28. Demos SG, Alfano RR. Optical polarization imaging. Appl Opt 1997;36:150–155. [PubMed: 18250656]
29. Elsner AE, Burns SA, Zhou Q, Dreher AW. Polarization modulation from in vivo human ocular fundus images (Abstract). Opt Photon News 1998;8:72.
30. Knighton RW, Huang XR. Analytical methods for scanning laser polarimetry. Opt Express 2002;10:1179–1189. [PubMed: 19451978]

31. Bueno JM. Polarimetry in the human eye using an imaging linear polariscope. J Optics A 2002;4:553–561.
32. Bueno JM, Campbell MCW. Confocal scanning laser ophthalmoscopy improvement by use of Mueller-matrix polarimetry. Opt Lett 2002;27:830–832. [PubMed: 18007942]
33. Elsner, AE.; Miura, M.; Stewart, JB.; Kairala, MBM.; Burns, SA. Novel algorithms for polarization imaging resulting in improved quantification of retinal blood vessels. In: Westwood, JD., editor. Medicine Meets Virtual Reality. Washington, DC: IOS Press; 2003. p. 59-61.
34. Dreher AW, Reiter K, Weinreb RN. Spatially resolved birefringence of the retinal nerve-fiber layer assessed with a retinal laser ellipsometer. Appl Opt 1992;31:3730–3735.
35. Weinreb RN, Dreher AW, Coleman A, Quigley H, Shaw B, Reiter K. Histopathologic validation of fourier-ellipsometry measurements of retinal nerve-fiber layer thickness. Arch Ophthalmol 1990;108:557–560. [PubMed: 2322159]
36. Van Blokland GJ, Verhelst SC. Corneal polarization in the living human eye explained with a biaxial model. J Opt Soc Am [A] 1987;4:82–90.
37. Bueno JM. Measurement of parameters of polarization in the living human eye using imaging polarimetry. Vision Res 2000;40:3791–3799. [PubMed: 11090671]
38. Knighton RW, Huang XR, Greenfield DS. Analytical model of scanning laser polarimetry for retinal nerve fiber layer assessment. Invest Ophthalmol Vis Sci 2002;43:383–392. [PubMed: 11818381]
39. Knighton RW, Huang XR. Linear birefringence of the central human cornea. Invest Ophthalmol Vis Sci 2002;43:82–86. [PubMed: 11773016]
40. Weinreb RN, Bowd C, Zangwill LM. Scanning laser polarimetry in monkey eyes using variable corneal polarization compensation. J Glaucoma 2002;11:378–384. [PubMed: 12362075]
41. Dreher AW, Reiter K. Retinal laser ellipsometry: a new method for measuring the retinal nerve-fiber layer thickness distribution. Clin Vision Sci 1992;7:481–488.
42. Ducros MG, Marsack JD, Rylander HG, Thomsen SL, Milner TE. Primate retina imaging with polarization-sensitive optical coherence tomography. J Opt Soc of Am [A] 2001;18:2945–2956.
43. Zhou Q, Weinreb RN. Individualized compensation of anterior segment birefringence during scanning laser polarimetry. Invest Ophthalmol Vis Sci 2002;43:2221–2228. [PubMed: 12091420]
44. Bour LJ, Lopes Cardozo NJ. On the birefringence of the living human eye. Vision Res 1981;21:1413–1421. [PubMed: 7314525]
45. Brink HBK, Vanblokland GJ. Birefringence of the human foveal area assessed in vivo with Mueller-matrix ellipsometry. J Opt Soc Am [A] 1988;5:49–57.
46. Blokland GJV, Norren DV. Intensity and polarization of light scattered at small angles from the human fovea. Vision Res 1986;26:485–494. [PubMed: 3727413]
47. Chipman, RA. Polarimetry. In: Bass, M.; van Stryland, EW.; Williams, DR.; Wolfe, WI., editors. The Handbook of Optics. New York: McGraw Hill; 1994. p. 1-27.
48. Morgan JE, Waldock A. Scanning laser polarimetry of the normal human retinal nerve fiber layer: a quantitative analysis. Am J Ophthalmol 2000;129:76–82. [PubMed: 10653416]
49. Brown B, Lovie-Kitchen J. Temporal function in age related maculopathy. Clin Exp Optom 1987;70.4:112–116.
50. Eisner A, Klein ML, Zilis JD, Watkins MD. Visual function and the subsequent development of exudative age-related macular degeneration. Invest Ophthalmol Vis Sci 1992;33:3091–3102. [PubMed: 1399412]
51. Mayer MJ, Spiegler SJ, Ward B, Glucs A, Kim CBY. Preliminary evaluation of flicker sensitivity as a predictive test for exudative age-related maculopathy. Invest Ophthalmol Vis Sci 1992;33:3150–3155. [PubMed: 1399420]
52. Sandberg MA, Gaudio AR. Slow photostress recovery and disease severity in age-related macular degeneration. Retina 1995;15:407–412. [PubMed: 8594633]
53. Sunness JS, Rubin GS, Applegate CA, et al. Visual function abnormalities and prognosis in eyes with age-related geographic atrophy of the macula and good visual acuity. Ophthalmology 1997;104:1677–1691. [PubMed: 9331210]
54. Remky A, Lichtenberg K, Elsner AE, Arend O. Short wavelength automated perimetry in age related maculopathy. Br J Ophthalmol 2001;85:1432–1436. [PubMed: 11734515]

55. Elsner AE, Burns SA, Weiter JJ. Cone photopigment in older subjects: decreased optical density in early age-related macular degeneration. J Opt Soc Am [A] 2002;19:215–222.
56. Bressler NM, Silva JC, Bressler SB, Fine SL, Green WR. Clinicopathologic correlation of drusen and retinal pigment epithelial abnormalities in age-related macular degeneration. Retina 1994;14:130–142. [PubMed: 8036323]
57. Sunness JS, Bressler NM, Maguire MG. Scanning laser ophthalmoscopic analysis of the pattern of visual loss in age-related geographic atrophy of the macula. Am J Ophthalmol 1995;119:143–151. [PubMed: 7530408]
58. Eisner A, Stoumbos VD, Klein ML, Fleming SA. Relations between fundus appearance and function. Invest Ophthalmol Vis Sci 1991;32:8–20. [PubMed: 1987108]
59. Sandberg MA, Weiner A, Miller S, Gaudio AR. High-risk characteristics of fellow eyes of patients with unilateral neovascular age-related macular degeneration. Ophthalmology 1998;105:441–447. [PubMed: 9499774]
60. Sommer A, Kues HA, D'Anna SA, Arkell S, Robin A, Quigley HA. Cross-polarization photography of the nerve fiber layer. Arch Ophthalmol 1984;102:864–869. [PubMed: 6732566]
61. Rowe MP, Pugh EN, Tyo JS, Engheta N. Polarization-difference imaging: a biologically inspired technique for observation through scattering media. Opt Lett 1995;20:608–610.
62. Tyo JS, Rowe MP, Pugh EN, Engheta N. Target detection in optically scattering media by polarization: difference imaging. Appl Opt 1996;35:1855–1870.
63. Cope WT, Wolbarsht ML, Yamanashi BS. The corneal polarization cross. J Opt Soc Am 1978;68:1139–1141. [PubMed: 712454]
64. Morgan JE, Waldock A, Jeffery G, Cowey A. Retinal nerve fibre layer polarimetry: histological and clinical comparison. Br J Ophthalmol 1998;82:684–690. [PubMed: 9797673]
65. Hartnett ME, Weiter JJ, Staurenghi G, Elsner AE. Deep retinal vascular anomalous complexes in advanced age-related macular degeneration. Ophthalmology 1996;103:2042–2053. [PubMed: 9003338]
66. Elsner AE, Moraes L, Beausencourt E, et al. Scanning laser reflectometry of retinal and subretinal tissues. Opt Express 2000;6:243–250. [PubMed: 19404357]
67. Remky A, Beausencourt E, Hartnett ME, Trempe CL, Arend O, Elsner AE. Infrared imaging of cystoid macular edema. Graefes Arch Clin Exp Ophthalmol 1999;237:897–901. [PubMed: 10541899]
68. Arend O, Remky A, Elsner AE, Bertram B, Reim M, Wolf S. Quantification of cystoid changes in diabetic maculopathy. Invest Ophthalmol Vis Sci 1995;36:608–613. [PubMed: 7890492]
69. Remky A, Arend O, Elsner AE, Toonen F, Wolf S, Reim M. Digital imaging of central serous retinopathy using infrared illumination. Ger J Ophthalmol 1995;4:203–206. [PubMed: 7492930]
70. Bille JF, Pelz B, Weschenmoser C, Goelz S, Fischer JP. Examination of the corneal birefringence in vivo with an electrooptical laser scanning ellipsometer. Phys Med 1997;13:308–312.
71. Pierscionek BK, Weale RA. Investigation of the polarization optics of the living human cornea and lens with Purkinje images. Appl Opt 1998;37:6845–6851. [PubMed: 18301501]
72. Bueno JM, Jaronski J. Spatially resolved polarization properties for in vitro corneas. Ophthalmic Physiol Opt 2001;21:384–392. [PubMed: 11563426]
73. Greenfield DS, Knighton RW, Huang XR. Effect of corneal polarization axis on assessment of retinal nerve fiber layer thickness by scanning laser polarimetry. Am J Ophthalmol 2000;129:715–722. [PubMed: 10926978]
74. Greenfield DS, Knighton RW, Feuer WJ, Schiffman JC, Zangwill L, Weinreb RN. Correction for corneal polarization axis improves the discriminating power of scanning laser polarimetry. Am J Ophthalmol 2002;134:27–33. [PubMed: 12095804]

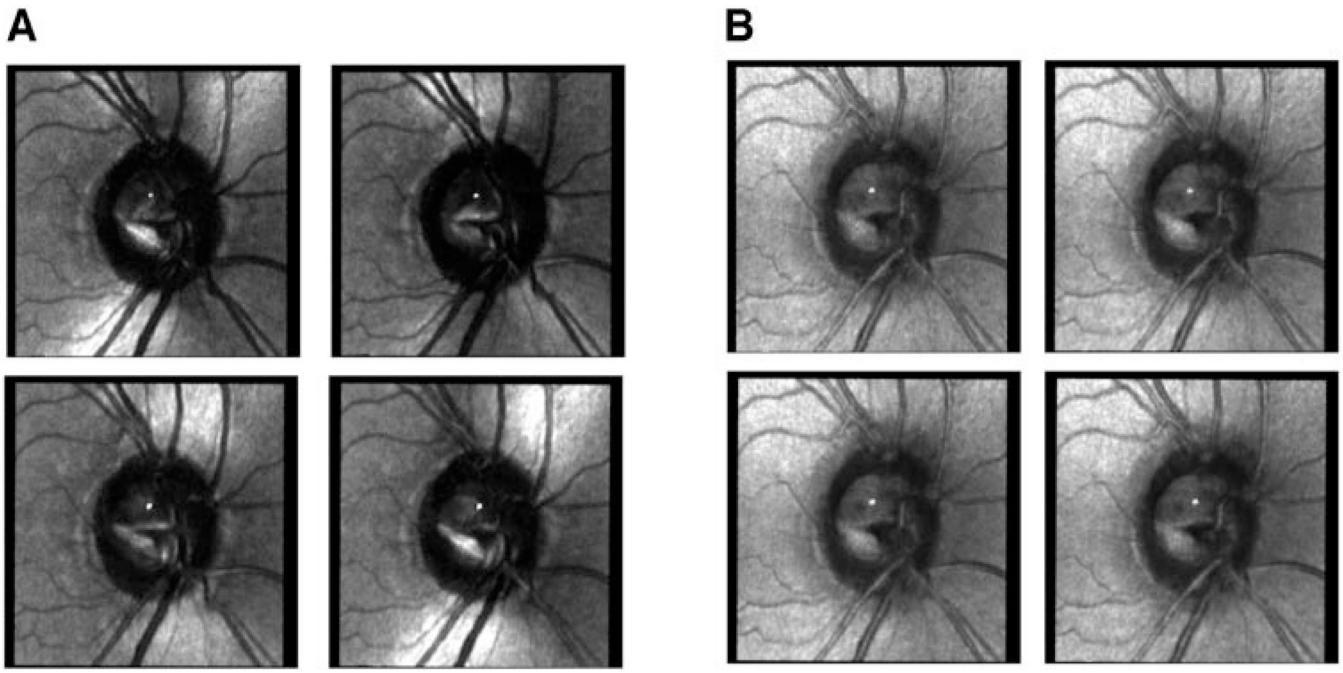


**Figure 1.**

Two sets of raw images of eyes with suspected glaucoma in a 46-year-old woman. Images were selected at equal intervals from the two sets of 20 images to show the effect of changing the polarization angle of the illumination on the image. (**A**) Four raw images from the crossed detector, showing the variation in the image for different input polarization angles. The features normally associated with specular reflections, such as the striped appearance of blood vessels, are not readily visible in these images. (**B**) Four raw images from the parallel polarized detector show that the variation in the image for different input polarization angles was less when compared with the overall intensity of the images. Features associated with specular reflections are readily visible.

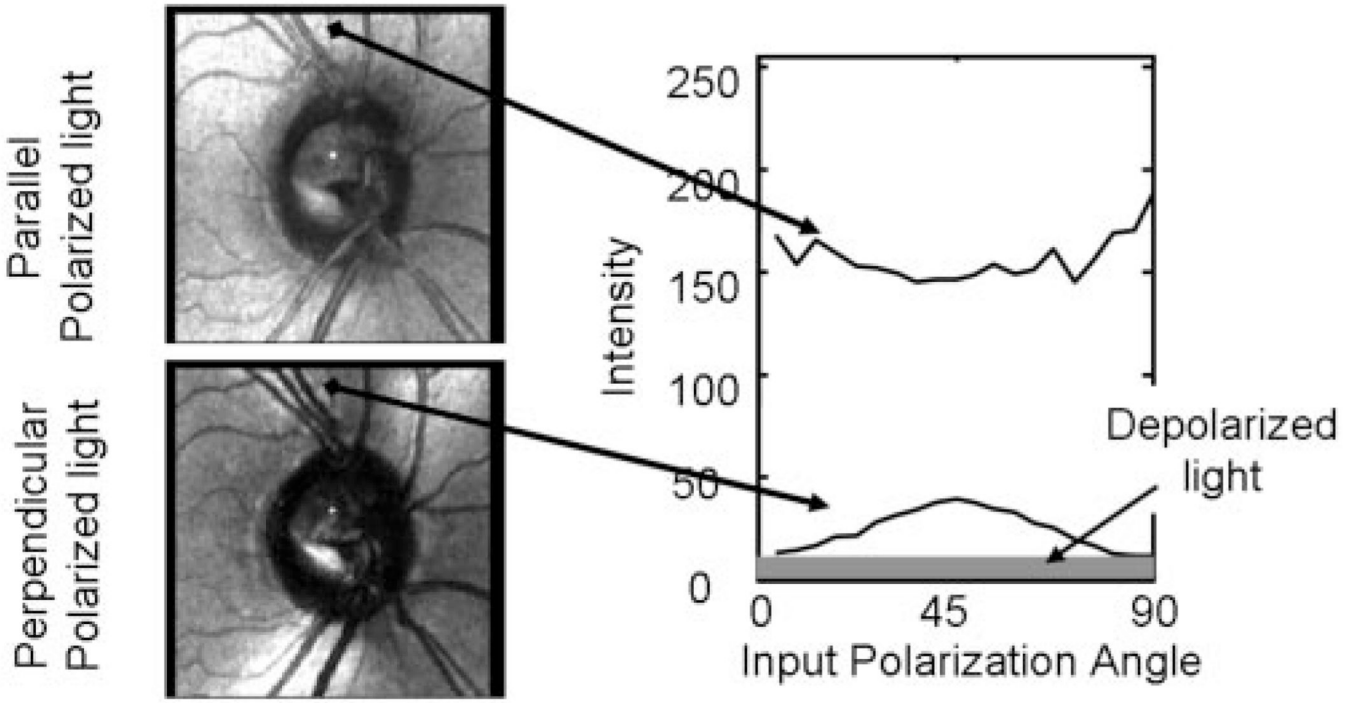


**Figure 2.**
Schematic diagram of the algorithm for computation of depolarized image. Two raw images from the patient in Figure 2, for the parallel detector (*top*) and the crossed polarized detector (*bottom*), showing the location of a region of interest. Intensity within the region of interest as a function of the input polarization.

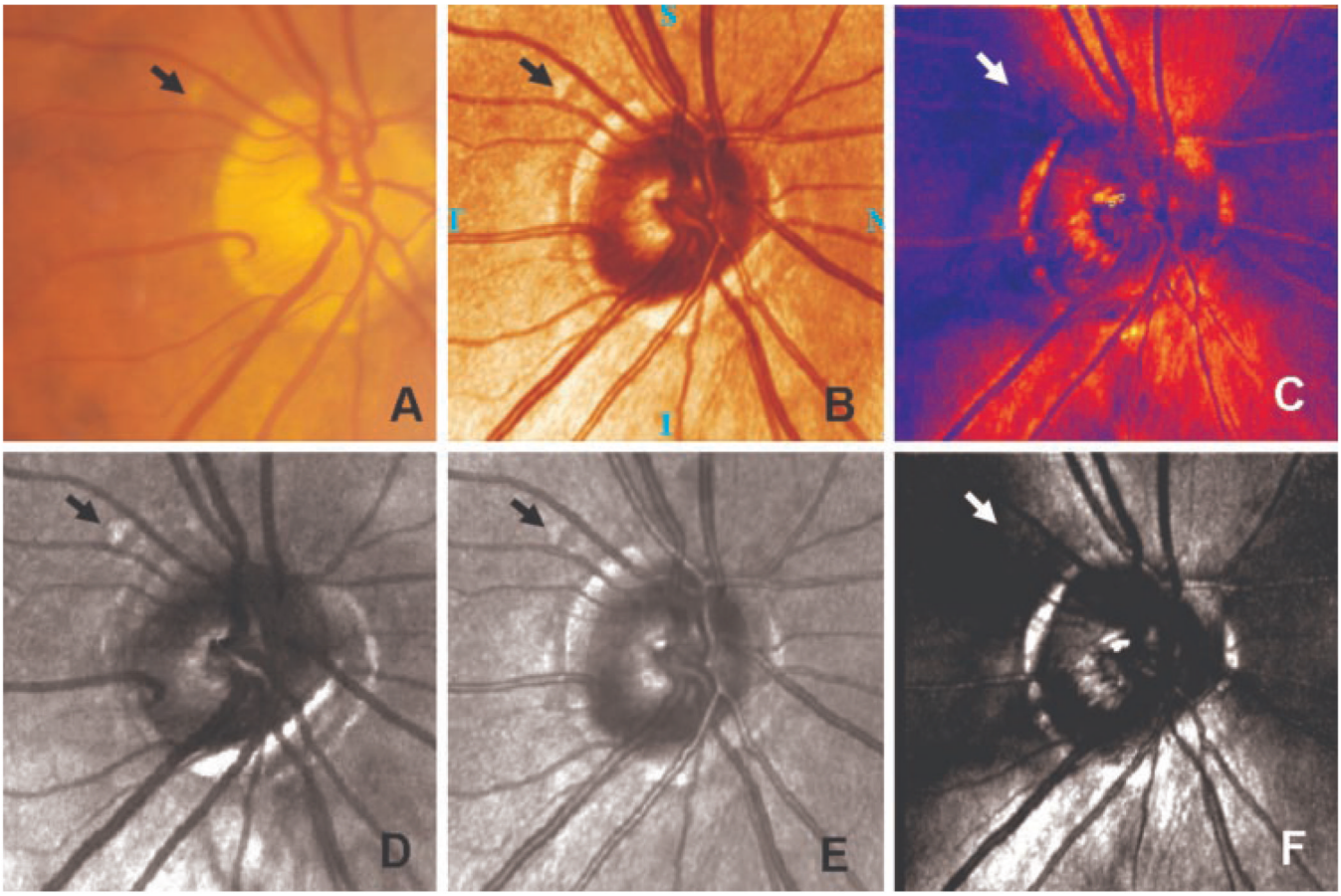


**Figure 3.**

A comparison of retinal images of a patient in the study. The druse in each image is indicated by an *arrow*. (**A**) Color fundus photograph. (**B**) A standard pseudocolor image of the retina from the standard GDx analysis. (**C**) The nerve fiber layer thickness map of the same region. (**D**) Depolarized light image. In addition to the druse, other nearby structures are evident. (**E**) Average grayscale image. (**F**) Polarization modulation image. Note that images (**B**) and (**E**), and (**C**) and (**F**), are essentially the same information, but the *top row* contains two images computed by the GDx software, and the *bottom row* shows the corresponding images computed with our analysis routines.

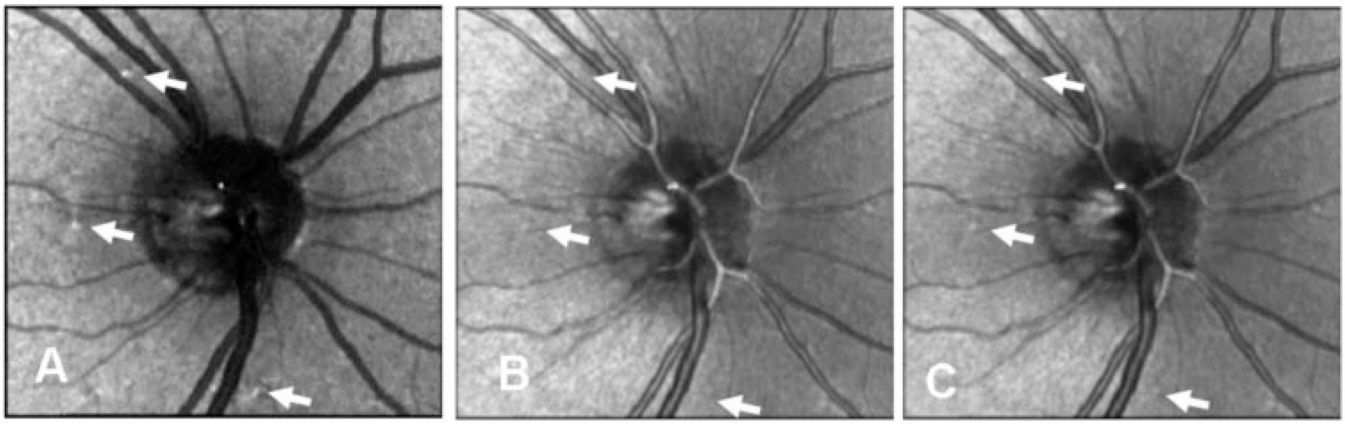


**Figure 4.**

Three computed images, centered on the optic nerve head and comparing the visibility of features, in a 61-year-old man with normal eyes. (**A**) Depolarized light image, (**B**) parallel polarized light image, and (**C**) average relative reflectance image. *Arrows*: actual sample locations for the statistical analysis. The comparison locations for computing contrast are adjacent to the sampled regions, but positioned to avoid other obvious structures such as blood vessels. These regions are not marked with arrows, because the arrows would overlap.

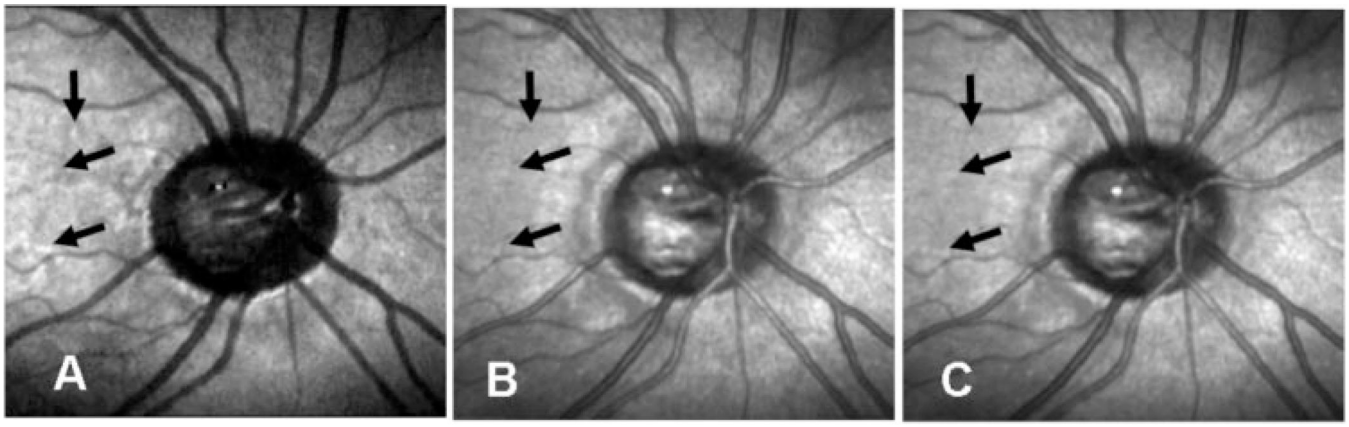


**Figure 5.**
Three computed images, as in Figure 4, for a 61-year-old woman with glaucoma. (**A**) Depolarized light image, (**B**) parallel polarized light image, and (**C**) average relative reflectance image. *Arrows*: actual sample locations for the statistical analysis.

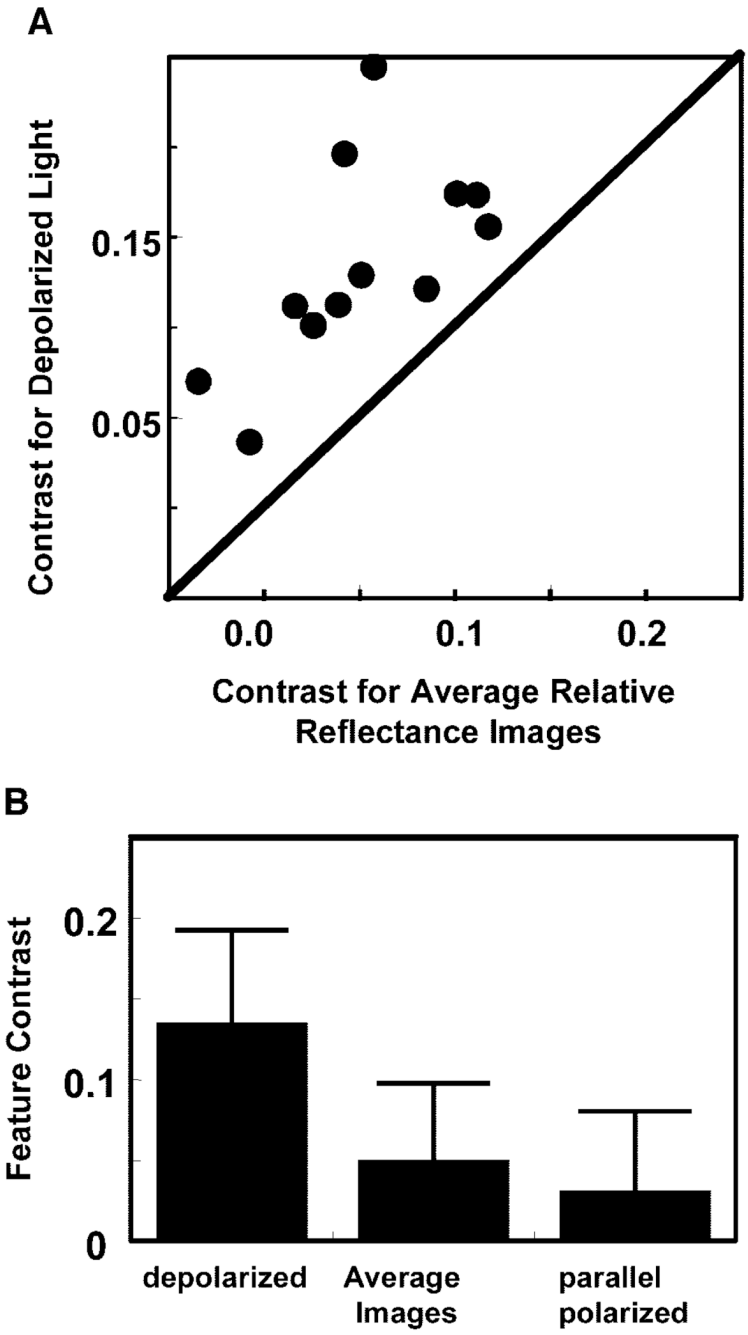


**Figure 6.**
Contrast of subretinal features in the images. (**A**) Michelson contrast of subretinal features for depolarized light and the average relative reflectance images. (**B**) Average feature contrast for all three image types. The contrast of features is greatest for depolarized light images. Error bars represent SDs of the contrasts.

**Table 1**

Summary of Clinical Data from the Subjects Included in the Analysis

| Patient | Age (y) | Eye | Sex | RE (sph eq) | IOP (mm Hg) | Clinical Diagnosis | HVF (OD/OS) |
|---|---|---|---|---|---|---|---|
| 1 | 61 | OD + OS | F | +1.00/pl | 16/14 | Glaucoma | Nasal step/paracentral scotoma |
| 2 | 59 | OD + OS | F | +1.00/+0.75 | 20/18 | Glaucoma | superior nasal step + sup defects OU |
| 3 | 54 | OD | F | −0.75 | 17 | Glaucoma OD | Double arcuate scotoma |
| 4 | 61 | OD + OS | M | pl/pl | 14/17 | Normal | Inferior nonspecific defects |
| 5 | 59 | OD + OS | F | pl/pl | 10/10 | Glaucoma | Superior arcuate/double arcuate scotoma |
| 6 | 61 | OD + OS | M | +1.25/+1.25 | 20/16 | Normal | Normal |
| 7 | 46 | OD | F | pl | 12 | Normal | Normal |

RE, refractive error; pl, plano; IOP, intraocular pressure; HVF, Humphrey visual field; OD, right eye; OS, left eye.